The ionospheric gravity and diamagnetic current systems

P. Alken,[1] S. Maus,[1] A. D. Richmond,[2] and A. Maute[2]

Received 31 August 2011; accepted 26 September 2011; published 10 December 2011.

[1] Large-scale currents in the ionosphere are driven by a variety of sources, including neutral winds, gravity, and plasma pressure gradients. While the stronger daytime wind-driven currents have been extensively studied, gravity and diamagnetic currents in the ionosphere have received very little attention but can have substantial effects even during the night. With the availability of a new generation of magnetic field models based on high-accuracy satellite magnetic measurements, it becomes increasingly important to account for these smaller current systems. In this work, we use the stand-alone NCAR TIEGCM electrodynamics solver along with empirical density, wind, and temperature inputs to model the global current systems caused by gravity and diamagnetism in the *F* region ionosphere and calculate their magnetic perturbations. These results allow us for the first time to visualize the global structure of these currents and quantify their magnetic perturbations. We find a significantly higher gravity-driven current during the night than one would expect from the lower conductivity which is primarily due to a Pedersen current driven by polarization charges in the predawn sector. We find some discrepancies between the diamagnetic perturbation and a theoretical prediction which could be a result of magnetic tension due to the curvature of the geomagnetic field lines. These results will allow geomagnetic field modelers to account for these important current systems and create more accurate models. This work will also be crucial in analyzing ionospheric magnetic field measurements from upcoming satellite missions such as Swarm.

Citation: Alken, P., S. Maus, A. D. Richmond, and A. Maute (2011), The ionospheric gravity and diamagnetic current systems, *J. Geophys. Res.*, *116*, A12316, doi:10.1029/2011JA017126.

1. Introduction

[2] The Earth's ionosphere is divided primarily into two layers, the *E* region from about 90 to 150 km altitude, and the *F* region from about 150 to 800 km altitude. In the *E* region, currents are mainly driven by neutral winds, resulting in large-scale dynamo currents, such as the equatorial electrojet and the midlatitude Sq current system. During the night, the *E* region typically disappears due to reduced ionization and its high recombination rate. In the higher-altitude *F* region, there are also dynamo currents driven by thermospheric winds [*Rishbeth*, 1971]. Wind generated electric fields in the *F* region are mapped along field lines to *E* region heights. Zonal winds cause vertical current flows at the equator which divert meridionally into both hemispheres at higher altitudes and then close equatorward at lower altitudes. These vertical *F* region dynamo currents have been detected in satellite data [*Maeda et al.*, 1982; *Lühr and Maus*, 2006]. Current systems also exist in the *F* region due to plasma effects. At the equator during daytime, zonal electric fields created by the global wind dynamo drive vertical ion drift, lifting plasma hundreds of kilometers upward, until gravity causes it to diffuse down magnetic field lines reaching an equilibrium roughly 15° on each side of the magnetic equator at *F* region altitudes. This density enhancement is called the Equatorial Ionization Anomaly (EIA).

[3] The EIA can enhance two important plasma currents which are of interest in this paper: the gravity-driven and diamagnetic currents. The gravity-driven current is caused by plasma interacting with the Earth's gravity and geomagnetic fields, while the diamagnetic current is driven by plasma pressure gradients. Due to the weak magnetic signature of both of these current systems (about 10,000 times smaller than the ambient geomagnetic field), it has historically been difficult to identify them in magnetic field measurements. However, these *F* region currents have been found to play an important role in ionospheric dynamics, particularly during nighttime. *Eccles* [2004] studied the *F* region gravity-driven and diamagnetic currents using a coupled ionosphere-electrodynamics model and found that the gravity-driven current contributes significantly to nighttime vertical drift velocities. *Maus and Lühr* [2006] first identified the gravity-driven current in satellite magnetic field observations, and found a large latitudinal range of current flowing. *Lühr et al.* [2003] first detected magnetic field depletions in satellite measurements which are due to the effects of the diamagnetic current. By assuming that the plasma pressure is exactly balanced by a change in magnetic pressure, they derived a

[1]National Geophysical Data Center, NOAA, Boulder, Colorado, USA.
[2]High Altitude Observatory, National Center for Atmospheric Research, Boulder, Colorado, USA.

0148-0227/11/2011JA017126

simple formula for the magnetic field depletion. This assumption is an approximation which neglects changes in magnetic tension, as we discuss later, and also neglects other forces parallel to the geomagnetic field, such as gravity and collisions with neutrals, which are important for balancing parallel pressure gradients. However, this assumption allows an estimation of diamagnetic corrections which are very important for high-accuracy geomagnetic field modeling [*Lühr and Maus*, 2010; *Maus et al.*, 2010]. In this paper, we further study these two important current systems using a modeling procedure based on both first principles and empirical inputs. Through this work, we are able to study the global flow of the gravity-driven and diamagnetic currents, as well as study the accuracy of the diamagnetic effect formula proposed by *Lühr et al.* [2003].

2. Ionospheric Currents

[4] Electric currents in the low and midlatitude ionosphere are primarily driven by winds, gravity and plasma pressure gradients. The expression for these currents is given by

$$\mathbf{J} = \sigma(\mathbf{E} + \mathbf{U} \times \mathbf{B}) + \mathbf{J}_g + \mathbf{J}_d \tag{1}$$

$$\mathbf{J}_g = \frac{nm_i}{B^2}\mathbf{g} \times \mathbf{B} \tag{2}$$

$$\mathbf{J}_d = \frac{1}{B^2}\mathbf{B} \times \nabla P \tag{3}$$

where σ is the conductivity tensor [*Forbes*, 1981, equation 10], $\mathbf{E}$ is the electric field, $\mathbf{U}$ is the neutral wind velocity field, n is the electron density, m_i is the ion mass, $\mathbf{g}$ is the gravitational acceleration, $\mathbf{B}$ is the ambient geomagnetic field with magnitude B, $P = nk(T_i + T_e)$ is the plasma pressure, k is the Boltzmann constant, T_i is the ion temperature, and T_e is the electron temperature. The first term on the right-hand side of equation (1) is responsible for the main ionospheric currents, including the equatorial electrojet and midlatitude Sq currents. These current systems are very prominent in the *E* region during the day but diminish significantly during the night due to a drop in *E* region conductivity. The second term $\mathbf{J}_g$ represents the gravity-driven current. This term depends on electron density n, and so we would expect this current to be strongest near the equatorial ionization anomaly (EIA) in the *F* region. Since the EIA is known to extend past the dusk terminator, this current could play a significant role during the night. The third term $\mathbf{J}_d$ represents the diamagnetic plasma current which flows in the presence of plasma pressure gradients. The diamagnetic current in a plasma in equilibrium arises from the balance between the plasma pressure force and the Lorentz force:

$$\nabla P = \mathbf{J} \times \mathbf{B} \tag{4}$$

Here, $P = nk(T_e + T_i)$ is the plasma pressure. Equation (4) arises from the standard magnetohydrodynamic equations for a plasma when assuming the net plasma flow acceleration is 0 (steady state), and ignoring gravity [*Chen*, 2006, equation 6–1]. We see immediately that in equilibrium, $\mathbf{B} \cdot \nabla P = \mathbf{J} \cdot \nabla P = 0$. This is an important statement, considering how complex the field and plasma distribution geometries may be. Crossing $\mathbf{B}$ into both sides of equation (4) and considering current flow perpendicular to $\mathbf{B}$ results in

$$\mathbf{J}_\perp = \frac{\mathbf{B} \times \nabla P}{B^2} \tag{5}$$

which is the diamagnetic current $\mathbf{J}_d$. It is called diamagnetic because it tends to flow in such a way as to diminish the ambient magnetic field. Understanding the diamagnetic current and resulting field in the ionosphere is very important for correcting magnetic measurements in geomagnetic field modeling [*Lühr and Maus*, 2010]. The diamagnetic current will also be concentrated near the EIA since that is where the plasma pressure gradients are greatest. *Lühr et al.* [2003] report magnetic field depletions of up to 5 nT at a variety of local times at CHAMP satellite altitude due to these currents. The $\mathbf{J}_g$ and $\mathbf{J}_d$ terms are strictly valid only when the ion collision frequency is small in comparison with the gyrofrequency about the magnetic field. Since both the gravity-driven and diamagnetic current systems are most prominent in the *F* region, where this condition is true, these terms are acceptable approximations of their respective currents.

[5] The gravity and diamagnetic currents cause secondary electric fields to build up which maintain a divergence-free current. These electric fields are contained in the first term of equation (1). Taking, for example, the gravity-driven current $\mathbf{J}_g = nm_i\mathbf{g} \times \mathbf{B}/B^2$, one can see that this expression is not necessarily divergence free for an arbitrary $\mathbf{B}$ and n, and so secondary electric fields will build up to ensure a divergence-free current, which will in turn close the flow of the gravity-driven current. A similar statement can be made for the diamagnetic term $\mathbf{J}_d$. Determining these secondary electric fields and their corresponding ionospheric currents is discussed in more detail in section 3. In section 4, we discuss our findings related to the gravity-driven current. In section 5, we present our model of the diamagnetic currents and their relation to the work of *Lühr et al.* [2003]. Finally we make some concluding remarks in section 6.

3. Modeling the *F* Region Currents With TIEGCM

[6] The NCAR TIEGCM (Thermosphere Ionosphere Electrodynamics General Circulation Model) [*Roble et al.*, 1988; *Richmond et al.*, 1992; *Richmond*, 1995] calculates self-consistently the dynamics, energetics, chemistry and electrodynamics of the ionosphere and thermosphere. While it would be possible to use the full model to compute the ionospheric currents, we found it preferable to use only the electrodynamic solver from TIEGCM, and use external empirical models for the needed ionospheric inputs. The TIEGCM electrodynamic solver calculates an electric potential Φ, and a corresponding electric field $\mathbf{E} = -\nabla\Phi$, which causes $\mathbf{J}$ in equation (1) to satisfy

$$\nabla \cdot \mathbf{J} = 0 \tag{6}$$

with suitable boundary conditions. Φ is generated by polarization charges which build up to ensure a divergence-free current. Assuming that the conductivity along geomagnetic field lines is very high, the electric field component in this direction is negligible, and so equation (6) reduces to a two-dimensional equation for the electric potential in magnetic

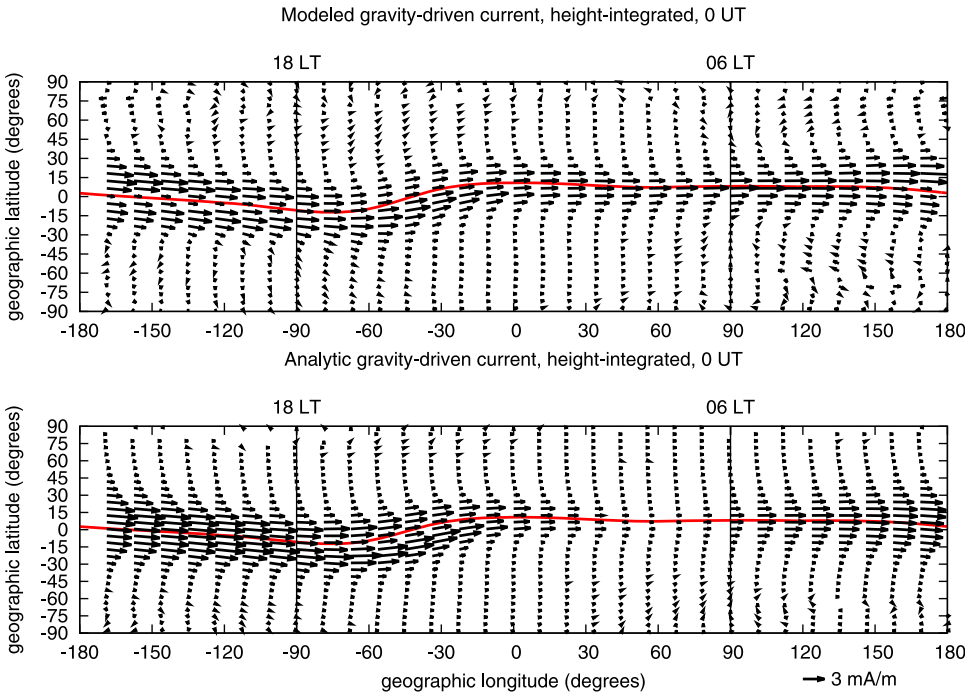

Figure 1. Height-integrated gravity-driven currents for (top) model calculation and (bottom) analytic term $\mathbf{J}_g$ for 0000 UT on 21 March 2003. Vertical lines indicate the positions of 0600 and 1800 local times. Red curve indicates position of the magnetic equator at 350 km altitude.

apex coordinates when integrated along magnetic field lines from the foot point at the base of the ionosphere in the southern hemisphere to the foot point in the northern hemisphere [*Richmond*, 1995, equation 5.23]. The high-latitude boundary condition, providing the coupling between the ionosphere and magnetosphere is provided by the convection model of *Heelis et al.* [1982]. The equatorial boundary condition is given by the condition that the meridional field-line-integrated current density must vanish [*Richmond*, 1995, equation 5.31].

[7] The remaining inputs to the electrodynamo solver are the ionospheric conductivities, neutral winds, and geomagnetic field. The conductivities rely on the ion, electron and neutral temperatures and densities. The density and temperature inputs for the electrons and ions were computed using the International Reference Ionosphere model IRI2007 [*Bilitza and Reinisch*, 2008]. IRI2007 provides climatologies of electron and ion densities and temperatures in the altitude range 50 km to 2000 km. The density and temperature inputs for the neutral particles were computed using the Mass Spectrometer Incoherent Scatter model NRLMSISE-00 [*Picone et al.*, 2002]. NRLMSISE-00 models climatological densities and temperatures of the neutral atmosphere from the Earth's surface to the exobase. The neutral wind velocity field was computed using the Horizontal Wind Model HWM07 [*Drob et al.*, 2008; *Emmert et al.*, 2008], which provides the climatologies of the zonal and meridional wind components. The geomagnetic field input was specified by the IGRF model [*Finlay et al.*, 2010].

[8] To facilitate the calculation of the ionospheric currents, we developed a subroutine to calculate the empirical densities, temperatures and winds using the above models, supply them to the TIEGCM electrodynamic solver, and isolate the gravity-driven and diamagnetic currents from the output. For the case of the gravity-driven current, this was accomplished by running the TIEGCM electrodynamic solver twice, once with all current terms provided, and once with the gravity term set to zero. By subtracting the latter solution from the former, we were able to isolate only the gravity contribution to the total current, accounting for the secondary electric fields built up. We isolated the diamagnetic current using the same procedure setting the corresponding term in the current equation to zero. Although current flows both perpendicular and parallel to **B**, we analyze only the larger perpendicular component in this study, since the parallel field-aligned currents are not yet computed by TIEGCM.

4. Features of the Gravity-Driven Current

[9] In Figure 1 (top), we plot the total gravity-driven current solution from our simulation for 0000 UT on 21 March 2003 using a solar radio flux index of F10.7 = 120, displaying the direction and magnitude of the current at each grid point with arrows. Figure 1 (top) shows the height-integrated horizontal component of the current perpendicular to **B** from 95 km to 640 km as a function of geographic latitude and longitude. We see that at low latitudes, the current is primarily magnetic eastward, following the dip equator. This is expected from the $\mathbf{g} \times \mathbf{B}$ term in the current. To illustrate the effect of the secondary polarization electric fields, we plot in Figure 1 (bottom) the height-integrated current flow $\mathbf{J}_g$. In Figure 1 (bottom) we see the current magnitude diminish significantly during the night, due to the lower electron density which gives rise to a divergent current. Figure 1 (top) does not have this feature, indicating the additional buildup

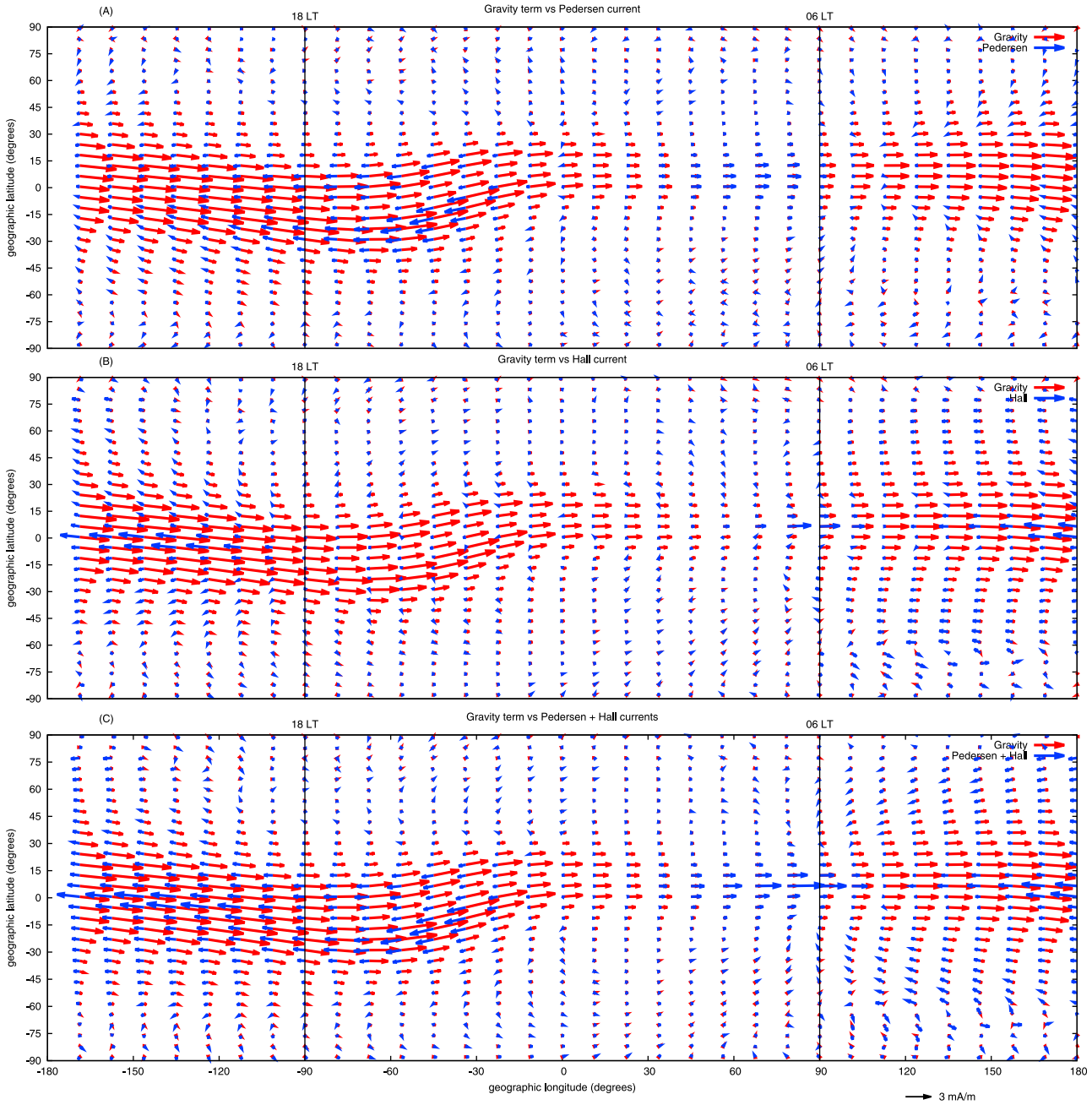

Figure 2. (a) $\mathbf{J}_g$ term (red) with Pedersen current derived from polarization electric field (blue). (b) $\mathbf{J}_g$ term (red) with Hall current derived from polarization electric field (blue). (c) $\mathbf{J}_g$ term (red) with sum of Pedersen and Hall currents derived from polarization electric field (blue). Figures 2a–2c represent height-integrated currents at 0000 UT on 21 March 2003.

of secondary electric fields in the predawn local time sector to maintain eastward current flow. One of the most important open questions regarding the gravity-driven current is the physical mechanism enabling it to close across this region of low conductivity.

[10] In a previous study, *Maus and Lühr* [2006] conjectured that the gravity-driven current would be restricted by its "bottleneck" of least ion density. Therefore, stronger currents on the dayside would be inhibited by weaker currents on the nightside. Interestingly, Figure 1 indicates that the nighttime current is stronger than one would expect from the low conductivity. This indicates the build up of strong polarization charges and induced electric fields to account for this stronger current. To investigate this further, we analyzed the polarization electric fields as computed by our simulation. We calculated the polarization electric fields due to the gravity-driven current by again running the model twice, once with all currents enabled and once with the gravity term turned off, and taking the difference. Then, the Pedersen and Hall conductivities along with the polarization electric field components enable the computation of the secondary currents. We are interested in whether a Pedersen or Hall current

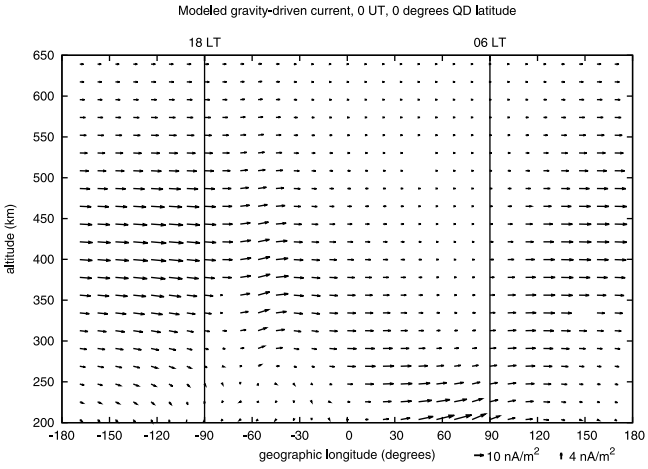

Figure 3. Gravity-driven current as a function of longitude and altitude for 0000 UT on 21 March 2003. Quasi-dipole latitude is held fixed at 0°. Vertical lines indicate the positions of 0600 and 1800 local times. Due to the much larger distance covered by the horizontal axis, two separate scaling factors were used in the vertical and horizontal directions as shown, in order to better visualize the current flow.

can explain the enhanced current feature seen in the predawn sector. The total gravity-driven current can be expressed as

$$\mathbf{J}_g^T = \sigma \mathbf{E}_g + \mathbf{J}_g = \sigma \mathbf{E}_g + \frac{nm_i}{B^2}\mathbf{g} \times \mathbf{B} \tag{7}$$

where $\mathbf{E}_g$ is the polarization electric field built up due to the divergent term $\mathbf{J}_g$. In Figure 2, we show the individual contributions from the $\mathbf{J}_g$ term and the Pedersen and Hall currents contributing to the $\sigma\mathbf{E}_g$ term:

$$\mathbf{J}_p = \sigma_p \mathbf{E}_g^{\perp} \tag{8}$$

$$\mathbf{J}_h = \sigma_h \hat{b} \times \mathbf{E}_g^{\perp} \tag{9}$$

where σ_p is the Pedersen conductivity, σ_h is the Hall conductivity, $\mathbf{E}_g^{\perp}$ is the polarization electric field component perpendicular to the magnetic field, and $\hat{b}$ is a unit vector in the direction of the magnetic field. Figure 2a shows $\mathbf{J}_g$ in red and the Pedersen current in blue. Here we see that in the predawn sector where $\mathbf{J}_g$ is small due to the low conductivity, the Pedersen current grows substantially to provide current flow across the dawn terminator. We also find in the local time region 1800–2200, the Pedersen current grows and opposes the flow of $\mathbf{J}_g$. Figure 2b shows $\mathbf{J}_g$ in red and the Hall current in blue. We see that the Hall current has a localized effect in the predawn sector which causes current flow across the dawn terminator, and opposes the gravity current flow during the daytime. The concentrated westward Hall current near the daytime magnetic equator is the modification of the equatorial electrojet current by the polarization electric field. Figure 2c shows the sum of the Pedersen and Hall currents in blue against $\mathbf{J}_g$ in red. The main conclusion of Figure 2 is that the daytime maximum of the $\mathbf{J}_g$ current does not flow uninterrupted into the night, nor does the lower nighttime extreme restrict the current during the day. Instead, an equilibrium current strength is reached between the two extremes, primarily enabled by the Pedersen current, but also aided by the Hall current. Built-up polarization charges are physically responsible for the fields driving these currents.

[11] To further explore the structure of this current system, we show in Figure 3 the gravity-driven current on the same day and UT, holding quasi-dipole latitude fixed at 0°. The arrows represent the vertical and longitudinal components of the total gravity-driven current flow $\mathbf{J}_g^T$. While we continue to see that the current flow is primarily eastward, interestingly it becomes stronger at lower altitudes as the night progresses. This is most likely due to the fact that the current is dominated by $\mathbf{J}_g$ in the evening, which peaks at a higher altitude, and by the Pedersen current in the early morning, peaking at a lower altitude. Looking at Figure 3 along with the latitudinal structure from Figure 1, it seems probable that there is a divergence of current perpendicular to **B** during the night. This indicates there could be an additional flow of current along magnetic field lines.

5. Features of the Diamagnetic Current

[12] In Figure 4 we plot the diamagnetic current flow calculated from our model at 15° geographic latitude and 1700 UT on 21 March 2003, overlayed on top of the electron density as provided by IRI. The arrows represent the vertical and longitudinal components of the total diamagnetic current flow $\mathbf{J}_d^T = \sigma\mathbf{E}_d + \mathbf{J}_d$, where $\mathbf{E}_d$ is the polarization electric field built up due to the divergent term $\mathbf{J}_d$. We see here the current flows around the density enhancement in a direction which will reduce the ambient geomagnetic field and is strongest in regions where the electron density changes most rapidly, as expected. One question of great interest is the magnitude of the magnetic field depletion resulting from this current. Knowledge of this depletion would aid greatly in correcting satellite measurements for highly accurate geomagnetic field

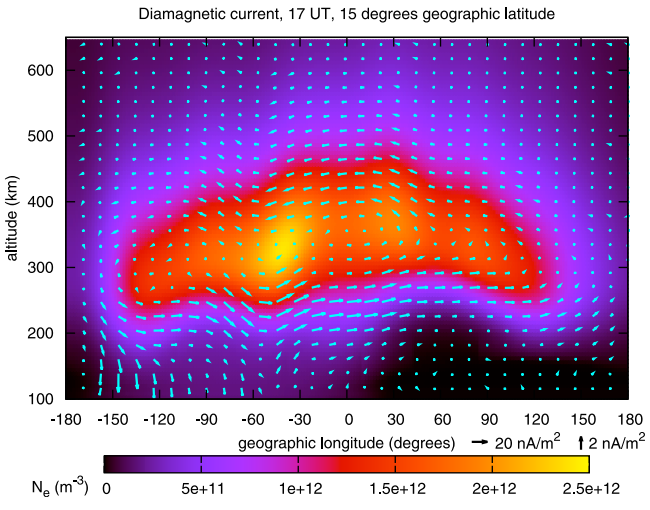

Figure 4. Diamagnetic current flow along with electron densities as a function of longitude and altitude for 1700 UT and 15° geographic latitude on 21 March 2003. Due to the much larger distance covered by the horizontal axis, two separate scaling factors were used in the vertical and horizontal directions as shown, in order to better visualize the current flow.

modeling. Combining Maxwell's equation $\nabla \times \mathbf{B} = \mu_0 \mathbf{J}$ with equation (4) yields the relation

$$\nabla\left(P + \frac{B^2}{2\mu_0}\right) = \frac{1}{\mu_0}(\mathbf{B}\cdot\nabla)\mathbf{B} \tag{10}$$

The left-hand side is the sum of plasma pressure and magnetic pressure forces, while the right-hand side represents magnetic tension due to the curvature of the field lines. By defining $\mathbf{B} = B\hat{b}$, we can show

$$\frac{1}{\mu_0}(\mathbf{B}\cdot\nabla)\mathbf{B} = \frac{d}{db}\left(\frac{B^2}{2\mu_0}\right)\hat{b} + \frac{B^2}{\mu_0}\frac{1}{R_c}\hat{n} \tag{11}$$

where b is a coordinate which varies along $\mathbf{B}$, $\hat{b}$ is the unit vector in the direction of $\mathbf{B}$, R_c is the radius of curvature of the field line, and $\hat{n} = R_c d\hat{b}/db$ is a vector normal to the field line and directed antiradially. We see that there will be a net tension if the field lines are curved or if the magnetic field strength varies along itself. *Lühr et al.* [2003] proposed a solution to equation (10) neglecting magnetic tension so the right-hand side would vanish, leading to a calculation of the parallel magnetic field perturbation due to the pressure P:

$$b_L = -\frac{\mu_0 P}{B_0} \tag{12}$$

Here, B_0 represents the unperturbed ambient field, and the negative sign indicates the ambient field magnitude is reduced. While equation (12) has been used to correct satellite magnetic measurements for modeling [*Lühr and Maus*, 2010], it remains an open question as to how accurate the formula is in the presence of curved field lines, as one finds in the Earth's geomagnetic field. To study this, we directly calculated the magnetic field resulting from the diamagnetic current computed by our model. This was done by first interpolating the current, represented in magnetic apex coordinates, to geographic spherical coordinates. The magnetic field of the resulting current was calculated using the toroidal and poloidal field decompositions of the current vector as described in detail by *Backus* [1986] and briefly discussed below.

[13] A solenoidal vector field $\mathbf{J}$ may be decomposed as

$$\mathbf{J} = \nabla \times \wedge\tilde{p} + \wedge\tilde{q} \tag{13}$$

$$\tilde{p}(r,\theta,\phi) = \nabla_1^{-2}(rJ_r) \tag{14}$$

$$\tilde{q}(r,\theta,\phi) = \nabla_1^{-2}(\wedge\cdot\mathbf{J}_s) \tag{15}$$

where $\wedge = \mathbf{r}\times\nabla$, $\nabla_1 = \nabla - \hat{r}\partial_r$, ∇_1^{-2} is the inverse of the operator ∇_1^2, $\mathbf{J}_s = \mathbf{J} - \hat{r}J_r$, and $\tilde{p}$ and $\tilde{q}$ are scalar functions representing the poloidal and toroidal components of $\mathbf{J}$, respectively. It can also be shown that $\wedge\cdot\mathbf{J}_s = \nabla\cdot(\mathbf{J}_s\times\mathbf{r})$.

[14] Applying the same decomposition to the magnetic field $\mathbf{B}$ and applying Maxwell's equation $\nabla\times\mathbf{B} = \mu_0\mathbf{J}$ yields

$$\mathbf{B} = \nabla\times\wedge p + \wedge q \tag{16}$$

$$q = \mu_0\tilde{p} \tag{17}$$

$$\nabla^2 p = -\mu_0\tilde{q} \tag{18}$$

The advantage of this method is $\tilde{p}$ and $\tilde{q}$ can be computed very efficiently using spherical harmonic expansions of rJ_r and $\wedge\cdot\mathbf{J}_s$ from equations (14) and (15), since the operator ∇_1^{-2} acting on a spherical harmonic Y_l^m simply produces a multiplicative factor of $-1/l(l+1)$. The toroidal magnetic field coefficients $q_l^m(r)$ are trivially related to $\tilde{p}_l^m(r)$ using equation (17) and so the main task is to solve for the poloidal magnetic field coefficients $p_l^m(r)$. Equation (18) leads to a Sturm-Liouville equation for the radial coefficients $p_l^m(r)$ which can be solved by means of Green's functions [*Engels and Olsen*, 1998, equation 9]:

$$p_l^m(r) = \int_a^b G_l(r,s)s^2\tilde{q}_l^m(s)ds \tag{19}$$

where

$$G_l(r,s) = \frac{1}{2l+1}\begin{cases}\left(\frac{r}{s}\right)^l\frac{1}{s} & r\le s\\ \left(\frac{s}{r}\right)^l\frac{1}{r} & r>s\end{cases} \tag{20}$$

and the integration is performed radially over the current region, defined by a spherical shell $S(a, b)$ (i.e., $\mathbf{J} = 0$ outside this shell). We solved the integrals in equation (19) by reformulating them in terms of an ordinary differential equation, and then using a Runge–Kutta solver. Defining

$$y_l^m(r,b) = \int_a^b G_l(r,s)s^2\tilde{q}_l^m(s)ds \tag{21}$$

we can construct an ODE system:

$$\frac{d}{ds}y_l^m(r,s) = G_l(r,s)s^2\tilde{q}_l^m(s) \tag{22}$$

$$y_l^m(r,a) = 0 \tag{23}$$

where the desired solution is

$$p_l^m(r) = y_l^m(r,b) \tag{24}$$

Equations (22) and (23) were solved using an adaptive step size eighth-order Runge–Kutta Prince-Dormand method. With the $p_l^m(r)$ and $q_l^m(r)$ known, equation (16) can be used to compute the magnetic field [see *Engels and Olsen*, 1998, equation 6]. The toroidal/poloidal decomposition method outlined above for computing magnetic fields is significantly superior to Biot-Savart type methods, both in terms of efficiency and accuracy, especially in the current region where Biot-Savart integrals contain a singularity.

[15] Once we calculated the magnetic field $\mathbf{B}_d^T$ from the diamagnetic current $\mathbf{J}_d^T$, in order to compare with equation (12), we computed the quantity

$$b_c = \mathbf{B}_d^T\cdot\frac{\mathbf{B}_0}{B_0} \tag{25}$$

This gives the component of the diamagnetic field in the direction of the ambient field which is the same quantity calculated by *Lühr et al.* [2003] for the nontension case. In

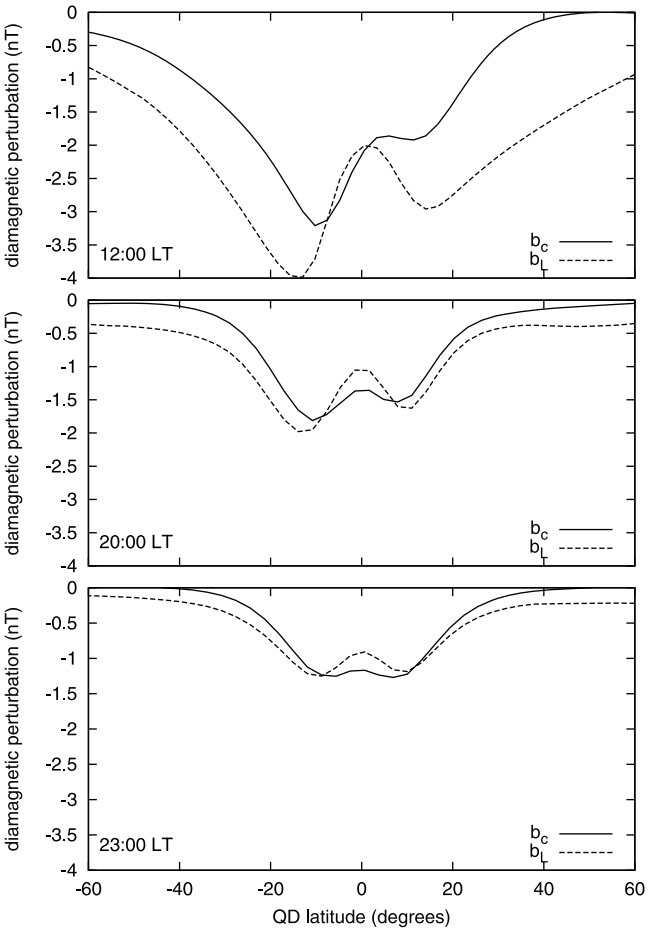

Figure 5. Calculated diamagnetic field (solid) perturbation with theoretical prediction (dashed) as a function of quasi-dipole latitude for 1700 UT on 21 March 2003, altitude 350 km for three different local times.

Figure 5 we plot b_c and b_L as a function of quasi-dipole latitude for three different local times on 21 March 2003 at an altitude of 350 km. The perturbations are negative, indicating the effect opposes the ambient geomagnetic field, as expected. We see both curves exhibit stronger effects near the anomaly density enhancements as expected, but the prediction of *Lühr et al.* [2003] differs significantly from the computed value at all latitudes.

[16] We are interested in whether this discrepancy is due to an error in the modeling or in the theoretical prediction. Since the theoretical prediction is strictly valid only when the ambient field (and the resulting diamagnetic field) have no curvature, we seek a system in equilibrium in a more complex field geometry with an analytical solution for comparison. *Krasheninnikov et al.* [1999] provide an explicit solution for the plasma pressure, diamagnetic current, and total magnetic field for a system in equilibrium in a dipole field geometry. In such a system, we would start with an ambient dipole field, supplied for example by a planetary magnetic field or in a laboratory by a small levitated current ring [*Hasegawa et al.*, 1990]. Plasma is then introduced to the system and the configuration is allowed to reach a steady state equilibrium. The resulting plasma profile, plasma current and total magnetic field are restated below and the reader is referred to *Krasheninnikov et al.* [1999] for more details. The plasma pressure is

$$P = P_0\left(\frac{R_0}{r}\right)^{2\alpha+4} h(x)^{2+4/\alpha} \tag{26}$$

where P_0 is the pressure at some reference surface which intersects the dipole equatorial plane at cylindrical radius R_0, $x = \cos\theta$, α is a constant related to the plasma β_0 = (plasma pressure)/(magnetic pressure) which is evaluated on the chosen reference surface. To evaluate the magnetic pressure on this surface, we choose B_R to be the magnetic field strength at R_0 on the dipole equatorial plane, so that $\beta_0 = 2\mu_0 P_0/B_R^2$. For plasmas with $\beta_0 \ll 1$, $\alpha = 1 - 512\beta_0/1001$. Finally, $h(x)$ is a function which satisfies the nonlinear dipole Grad-Shafranov equation and in the small β_0 limit is given by

$$\frac{h(x)}{1-x^2} = 1 - \frac{192}{1001}\beta_0 \sum_{i=1}^{5} c_i\left[1-\left(1-x^2\right)^i\right] \tag{27}$$

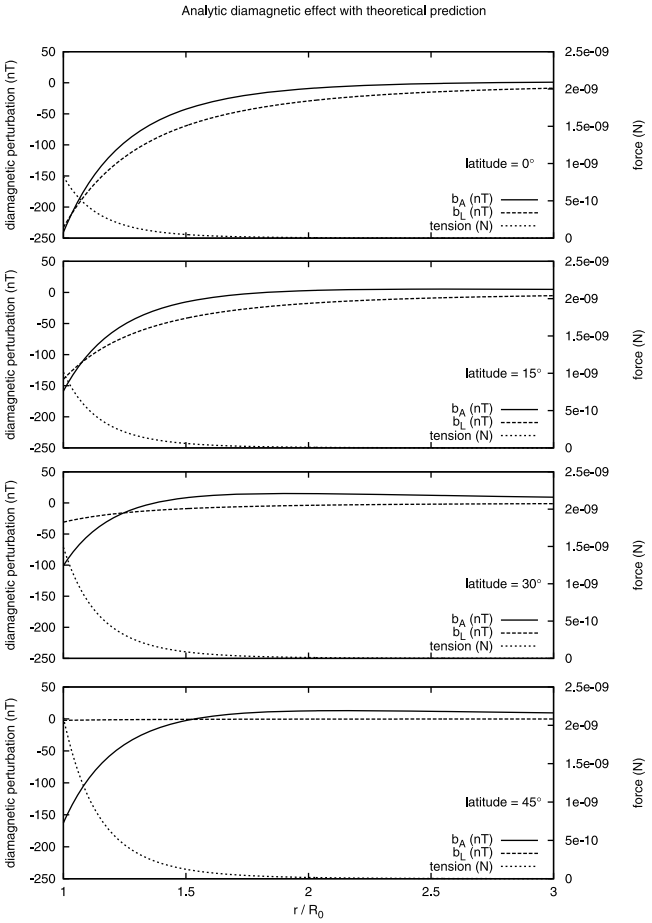

Figure 6. Analytic diamagnetic field perturbation (b_A, solid) with theoretical prediction (b_L, dashed) for dipole equilibrium test case, plotted as a function of r/R_0 for four different latitudes. Tension force magnitude (dotted) plotted on second vertical axis.

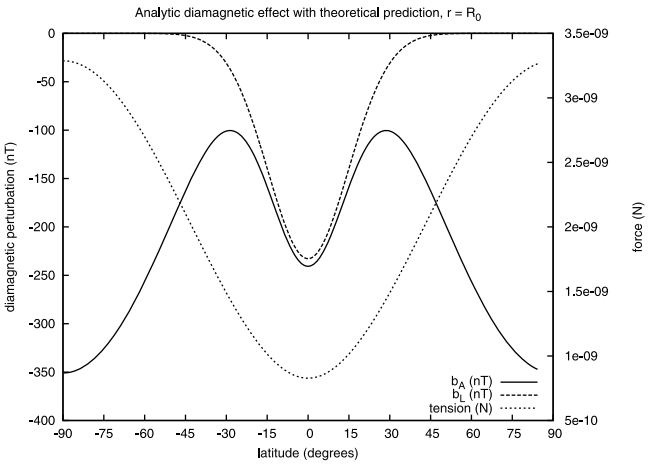

Figure 7. Analytic diamagnetic field perturbation (b_A, solid) with theoretical prediction (b_L, dashed) for dipole equilibrium test case, plotted as a function of latitude for $r = R_0$. Tension force magnitude (dotted) plotted on second vertical axis.

with the coefficients $c_i = \left(1, \frac{5}{12}, \frac{35}{144}, \frac{21}{128}, \frac{77}{640}\right)$ [*Krasheninnikov et al.*, 1999, equations 12 and 15]. The diamagnetic current and total magnetic field are then given by

$$\mathbf{J} = \frac{\beta_0(2+\alpha)B_R R_0^{\alpha+2}\sin\theta}{\mu_0 r^{\alpha+3}} h(x)^{1+4/\alpha}\hat{\phi} \tag{28}$$

$$\mathbf{B} = \frac{B_R R_0^{\alpha+2}}{\alpha r^{\alpha+2}}\left[\hat{\theta}\frac{\alpha h}{\sin\theta} - \hat{r}\frac{dh}{dx}\right] \tag{29}$$

It can be verified that the MHD equilibrium equations and Maxwell's equations are satisfied by this field and plasma configuration. We see that in the vacuum limit, $\beta_0 \rightarrow 0$, $\alpha \rightarrow 1$, $\mathbf{J} \rightarrow 0$, $h \rightarrow \sin^2\theta$ and $\mathbf{B}$ reduces to a simple dipole field. This field can be expressed as

$$\mathbf{B}_v = \frac{F}{2\pi}\frac{R_0}{r^3}\left[\sin\theta\hat{\theta} + 2\cos\theta\hat{r}\right], \tag{30}$$

where $F = 2\pi R_0^2(B_R/\alpha)$ is the magnetic flux through the dipole equatorial plane for $r > R_0$. If we consider R_0 to be representative of the mean height of the ionosphere, it is more physically realistic to hold the flux F constant than B_R when analyzing the vacuum limit, because the field strength in the equatorial ionosphere is not constant when plasma pressure changes, but the displacement of magnetic flux out of the ionosphere by plasma pressure does tend to reduce the ionospheric field and increase the field at high altitudes in a manner analogous to the model of *Krasheninnikov et al.* [1999]. The analytical field depletion due to the diamagnetic current can now be defined as

$$b_A = |\mathbf{B}| - |\mathbf{B}_v| \tag{31}$$

[17] This can be directly compared with equation (12), where $B_0 = |\mathbf{B}_v|$. In Figure 6 we plot the analytic result b_A against the theoretical prediction b_L as a function of r/R_0 for our test case for four different latitudes with the following parameters: $\beta_0 = 0.01$, $F = 1.2 \times 10^{10}$Wb, $R_0 = R_E = 6371.2$km. We also plot the magnitude of the tension force (the RHS of equation (10)) on the second vertical axis. We see that in the equatorial region, where the tension magnitude is smallest, b_L has the best agreement with b_A. The agreement in the 30° and 45° latitude plots is significantly worse, since the magnetic tension is higher. In these plots, the b_L prediction of *Lühr et al.* [2003] is small in magnitude, primarily due to the plasma pressure P dropping off very rapidly at high latitudes. To further illustrate the effect, we plot in Figure 7 the analytic result b_A against the theoretical prediction b_L as a function of latitude, holding r fixed at R_0. Magnetic tension is again plotted on the second vertical axis. We find good agreement at low latitudes where the tension is minimum, and significant disagreement at mid and high latitudes where tension is large. Since the Earth's geomagnetic field has a large dipole moment, it is likely that magnetic tension plays a significant role in the ionospheric diamagnetic effect and cannot be ignored.

6. Conclusion

[18] We have successfully modeled the *F* region gravity-driven and diamagnetic current systems using the NCAR TIEGCM model with empirical density, wind and temperature inputs. The global gravity-driven current structure exhibits a strong eastward flow at low latitudes primarily following the equatorial ionization anomaly as expected. The current strength during the night is significantly higher than expected from the low conductivity, but not as high as the strongest local daytime current magnitude as computed from $\mathbf{J}_g$. This is due to the buildup of significant polarization electric fields in the predawn sector as well as during the day. During the night, the gravity-driven current strength descends in altitude and diverges perpendicular to $\mathbf{B}$, implying that there is also a significant field-aligned current, which is not currently calculated. The diamagnetic current structure has also been presented, which is also prominent near the EIA. The magnitude of its ambient field depletion has been calculated by directly computing its magnetic field. These field depletions were compared with the theoretical prediction of *Lühr et al.* [2003] with significant discrepancies. These discrepancies could be due to magnetic tension of the curved geomagnetic field, which was not accounted for by the theoretical prediction. They could also be due to inaccuracies in the TIEGCM modeling, such as the neglect of the influence of parallel currents, which we plan to investigate in a future study. With this modeling framework in place, the next step will be to compare satellite data with our modeling predictions to determine the model's accuracy. The benefits of having an accurate ionospheric current model include creating more accurate ionospheric magnetic field models, as well as gaining the ability to further analyze high-accuracy magnetic field measurements from future satellite missions.

[19] **Acknowledgments.** This work was supported in part by NASA grant NNX08AG09G. The National Center for Atmospheric Research is sponsored by the National Science Foundation. We would also like to thank Wenbin Wang for helpful comments on an earlier draft.

[20] Robert Lysak thanks the reviewers for their assistance in evaluating this paper.

References

Backus, G. (1986), Poloidal and toroidal fields in geomagnetic field modeling, *Rev. Geophys.*, *24*(1), 75–109.

Bilitza, D., and B. W. Reinisch (2008), International Reference Ionosphere 2007: Improvements and new parameters, *Adv. Space Res.*, *42*(4), 599–609, doi:10.1016/j.asr.2007.07.048.

Chen, F. F. (2006), Introduction to Plasma Physics and Controlled Fusion, vol. 1, *Plasma Physics*, 2nd ed., Springer, New York.

Drob, D. P., et al. (2008), An empirical model of the Earth's horizontal wind fields: HWM07, *J. Geophys. Res.*, *113*, A12304, doi:10.1029/2008JA013668.

Eccles, J. V. (2004), The effect of gravity and pressure in the electrodynamics of the low-latitude ionosphere, *J. Geophys. Res.*, *109*, A05304, doi:10.1029/2003JA010023.

Emmert, J. T., D. P. Drob, G. G. Shepherd, G. Hernandez, M. J. Jarvis, J. W. Meriwether, R. J. Niciejewski, D. P. Sipler, and C. A. Tepley (2008), DWM07 global empirical model of upper thermospheric storm-induced disturbance winds, *J. Geophys. Res.*, *113*, A11319, doi:10.1029/2008JA013541.

Engels, U., and N. Olsen (1998), Computation of magnetic fields within source regions of ionospheric and magnetospheric currents, *J. Atmos. Sol. Terr. Phys.*, *60*, 1585–1592.

Finlay, C. C., et al. (2010), International Geomagnetic Reference Field: The eleventh generation, *Geophys. J. Int.*, *183*(3), 1216–1230, doi:10.1111/j.1365-246X.2010.04804.x.

Forbes, J. M. (1981), The equatorial electrojet, *Rev. Geophys.*, *19*(3), 469–504.

Hasegawa, A., L. Chen, and M. Mauel (1990), A D-^{3}He fusion reactor based on a dipole magnetic field, *Nucl. Fusion*, *30*, 2405–2413.

Heelis, R., J. Lowell, and R. Spiro (1982), A model of the high-latitude ionospheric convection pattern, *J. Geophys. Res.*, *87*, 6339–6345.

Krasheninnikov, S. I., P. J. Catto, and R. D. Hazeltine (1999), Magnetic dipole equilibrium solution at finite plasma pressure, *Phys. Rev. Lett.*, *82*(13), 2689–2692.

Lühr, H., and S. Maus (2006), Direct observation of the *F* region dynamo currents and the spatial structure of the EEJ by CHAMP, *Geophys. Res. Lett.*, *33*, L24102, doi:10.1029/2006GL028374.

Lühr, H., and S. Maus (2010), Solar cycle dependence of quiet-time magnetospheric currents and a model of their near-Earth magnetic fields, *Earth Planets Space*, *62*, 843–848.

Lühr, H., M. Rother, S. Maus, W. Mai, and D. Cooke (2003), The diamagnetic effect of the equatorial Appleton anomaly: Its characteristics and impact on geomagnetic field modeling, *Geophys. Res. Lett.*, *30*(17), 1906, doi:10.1029/2003GL017407.

Maeda, H., T. Iyemori, T. Araki, and T. Kamei (1982), New evidence of a meridional current system in the equatorial ionosphere, *Geophys. Res. Lett.*, *9*, 337–340.

Maus, S., and H. Lühr (2006), A gravity-driven electric current in the Earth's ionosphere identified in CHAMP satellite magnetic measurements, *Geophys. Res. Lett.*, *33*, L02812, doi:10.1029/2005GL024436.

Maus, S., C. Manoj, J. Rauberg, I. Michaelis, and H. Lühr (2010), NOAA/NGDC candidate models for the 11th generation International Geomagnetic Reference Field and the concurrent release of the 6th generation Pomme magnetic model, *Earth Planets Space*, *62*, 729–735.

Picone, J. M., A. E. Hedin, D. P. Drob, and A. C. Aikin (2002), NRLMSISE-00 empirical model of the atmosphere: Statistical comparisons and scientific issues, *J. Geophys. Res.*, *107*(A12), 1468, doi:10.1029/2002JA009430.

Richmond, A. D. (1995), Ionospheric electrodynamics using magnetic apex coordinates, *J. Geomagn. Geoelectr.*, *47*, 191–212.

Richmond, A. D., E. C. Ridley, and R. G. Roble (1992), A thermosphere/ionosphere general circulation model with coupled electrodynamics, *Geophys. Res. Lett.*, *6*, 601–604.

Rishbeth, H. (1971), The *F*-layer dynamo, *Planet. Space Sci.*, *19*, 263–267.

Roble, R. G., E. C. Ridley, A. D. Richmond, and R. E. Dickinson (1988), A coupled thermosphere/ionosphere general circulation model, *Geophys. Res. Lett.*, *15*, 1325–1328.

P. Alken and S. Maus, National Geophysical Data Center, NOAA E/GC1, 325 Broadway, Boulder, CO 80305-3328, USA. (patrick.alken@noaa.gov)

A. Maute and A. D. Richmond, High Altitude Observatory, National Center for Atmospheric Research, Boulder, CO 80307, USA.